Spatialization of saturated hydraulic conductivity using the Bayesian Maximum Entropy method: Application to wastewater infiltration areas

Sara Rabouli, Marc Serre, Vivien Dubois, Julien Gance, Hocine Henine, Pascal Molle, Catherine Truffert, Laura Delgado-Gonzalez, Rémi Clément

Title: Vertical 2D spatialization of saturated hydraulic conductivity by integrating ERT and infiltration test into a Bayesian Maximum Entropy data fusion method: Application to wastewater infiltration area

Authors:

Sara Rabouli [(1)], Marc Serre [(2)], Vivien Dubois [(1)], Julien Gance [(3)], Hocine Henine [(4)], Pascal Molle [(1)], Catherine Truffert [(3)], Laura Delgado-Gonzalez [(1)], Rémi Clément [(1)]

1) INRAE, REVERSAAL, F-69626 Villeurbanne Cedex, France

2) University of North Carolina, Chapel Hill, NC, USA

3) IRIS Instruments, 45100 Orléans, France

4) INRAE, UR HYCAR, 1 Rue Pierre Gilles de Gennes, 92160 Antony

Corresponding author: sara.rabouli@inrae.fr

Abstract:

Wastewater treatment, a major issue at the European level, focuses on improving surface and groundwater quality, preserving the receiving environment and ensuring a sustainable use of water. Soil infiltration is increasingly practiced downstream of wastewater treatment plants, particularly in rural areas without surface water bodies, as is the use of soil as an additional buffer and treatment step. However, the design of infiltration areas on heterogeneous soils remains an extremely complex task due to the costly and time-consuming spatial measurement of saturated hydraulic conductivity (Ks). This article proposes integrating 2D electrical resistivity tomography and infiltration tests into a Bayesian Maximum Entropy method, yielding a vertical mapping of soil heterogeneities at a metric scale. This updated method will facilitate infiltration area design in a heterogeneous soil setting.

Keywords:

Wastewater treatment plant, design, Bayesian Maximum Entropy, saturated hydraulic conductivity, electrical resistivity tomography, infiltration test.

1. Introduction

Despite the advances achieved in wastewater treatment plants over the last few decades, treated wastewater (TWW) can still exert a strong impact on downstream receiving rivers (Aubertheau *et al*., 2017). This is especially true in French rural areas, where treatment plants are mainly dedicated to treating carbonaceous pollution due to their small capacities (< 1,000 population equivalent, (MEDDE, 2015)). Consequently, the application of an extensive process like soil infiltration has become increasingly practiced as an option to provide tertiary treatment; it consists of TWW discharge over a large surface area (trenches, ponds, basins or meadows), allowing for gradual infiltration through the soil. The pollutants (nitrogen and phosphorus) are naturally treated by biodegradation processes or retained in the soil. The design and management of a TWW infiltration area is mainly based on an estimation of the soil saturated hydraulic conductivity (Ks) in order to calculate the discharge capacity and evaluate its treatment potential (Siegrist, 2014). However, Ks remains one of the most difficult soil properties to determine (Mahapatra *et al*., 2020) and its spatial variability can significantly influence TWW infiltration (Zhang *et al.*, 2019). Infiltration tests are usually carried out using the Porchet constant head method, which outputs direct and local measurements of Ks and requires 1 to 4 hours per test depending on the soil type. For heterogeneous soils, the estimation of Ks requires numerous measurements to establish confident predictions of TWW discharge (Warrick *et al*., 1977); this protocol can prove to be invasive and time-consuming. Nevertheless, an incorrect estimations of Ks could lead to malfunctions in the TWW infiltration areas via: i) premature clogging (McKinley and Siegrist, 2011), ii) over-infiltration and groundwater contamination, and iii) under-infiltration leading to puddling and olfactory nuisances (Morugán-Coronado *et al.*, 2011).

For the estimation of Ks variability, Bisone *et al*. (2017) proposed using geophysical methods on TWW infiltration areas with a subjective delineation of heterogeneity in order to locate a few infiltration tests for an optimal design. Geophysical methods allow visualizing soil structures through the measurement of a given physical parameter (wave speed, electrical resistivity (ER), elasticity)

(Romero-Ruiz *et al.*, 2018). Such methods are non-intrusive and yield physical information on large soil volumes yet still involve significant uncertainties (Loke *et al*., 2013). In the environmental sciences for near-surface (0-2 m) investigations, electrical resistivity tomography (ERT) is a widely used method whenever 2D vertical information is required (Hellman *et al.*, 2017).

The ER signal is a function of a number of soil properties, including: the nature of solid constituents (particle size and distribution), the arrangement of voids (porosity, pore size distribution, connectivity), water content, the ER of the fluid, and the temperature (Samouëlian *et al.*, 2005; Telford *et al.*, 1990). On the other hand, the ER signal has no direct dependence on Ks (Attwa and Ali, 2018; Weller and Slater, 2019); their physical relationship tends to be specific to the given soil type and is difficult to transpose directly to heterogeneous soils (Doussan and Ruy, 2009).

Only a few articles have explored the notion of using ERT to determine soil Ks with ER. Two approaches were found to be extremely attractive: the first employs empirical relationships between ER and Ks (Vogelgesang *et al.*, 2020), while the second adds a hydrodynamic model constrained by geophysics during the inversion process (Farzamian *et al.*, 2015). The former is a simple method yet still generates a high level of Ks estimation uncertainty, whereas the latter is probably the most robust method but requires an extensive numerical approach and tends not to be well adapted to TWW infiltration area design.

The 2D estimation of Ks from geophysical measurements and point measurements necessitates the use of other emerging methods for simple and robust applications, e.g. data fusion methods (Dezert *et al.*, 2019; Li *et al.*, 2019). Data fusion refers to the process of integrating multiple data sources in order to produce more accurate and useful information. Until now, no paper has yet to be published regarding data fusion between ERT and Ks.

Among all data fusion methods, Bayesian Maximum Entropy (BME) seems to be the best adapted in considering the datasets: ERT data (dense with high uncertainty, hard data), and infiltration data (reliable but sparse, soft data) (Christakos *et al.*, 2002). BME is a nonlinear spatial estimator that

rigorously accounts for spatial variability and the non-Gaussian characteristic of uncertain data (here, uncertainty is represented by a variance). Christakos *et al.* (2002) showed that BME is a relevant method for predicting spatial data encompassing several environmental parameters. For instance, it has been successfully used to predict water table variations (D'Or *et al.*, 2001) and estimate soil salinity (Douaik *et al.*, 2005). These examples suggest that the BME method is suitable to estimate 2D-Ks maps. The aim of this paper is to merge Ks and ERT measurements in order to obtain the most accurate estimation of Ks, thus providing new TWW infiltration area design elements.

2. Materials and methods

2.1. General methodology

The methodology adopted herein to evaluate the benefit of BME is based on a classical approach widely used in the geophysical literature (Radulescu *et al.*, 2007); it is composed of three steps:

- The first step consists of constructing synthetic datasets based on three synthetic Ks reference models (Ks_{ref}), and then simulating the ERT measurements and infiltration tests for each model.
- The second step adapts, evaluates and determines the BME method limits by means of the numerical datasets created in the previous step, through:
    - Defining the optimal number of hard data points (14, 24 or 50) for a homogeneous Water Content (WC) of 0.25-$m^3.m^{-3}$;
    - Validating a robust sampling strategy of hard data;
    - Assessing the impact of soil moisture variation in the model.
- The third step validates the BME method on a field dataset.

2.2. Datasets

2.2.1 Synthetic datasets

The synthetic datasets generated from Ks_{ref} (Figure 1a) are organized into both hard and soft data. Soft data generation consists of simulating the geophysical measurement and deriving hydraulic

conductivity, denoted $\mathrm{Ks}_{\mathrm{Geo}}$, from ERT (Figure 1b). Hard data, on the other hand, are local estimations of Ks sampled directly from Ks_{ref}; these data correspond to a simulation of the infiltration tests (Figure 1c). As for $\mathrm{Ks}_{\mathrm{Geo}}$, the first step entails simulating soil WC based on groundwater flow modeling, which will provide a realistic soil WC data distribution (Section 2.2.1.2.1). In taking WC and soil type into account, petrophysical relationships drawn from the literature will be used to calculate true electrical resistivity $\mathrm{ER}_{\mathrm{True}}$ (Section 2.2.1.2.2) and simulate apparent electrical resistivity ($\mathrm{ER}_{\mathrm{App}}$) for each Ks model (Section 2.2.1.2.3.1); next, we will invert $\mathrm{ER}_{\mathrm{App}}$ data to obtain interpreted electrical resistivity ($\mathrm{ER}_{\mathrm{Interp}}$) (Section 2.2.1.2.3.2). Lastly, $\mathrm{ER}_{\mathrm{Interp}}$ data will be transformed into $\mathrm{Ks}_{\mathrm{Geo}}$ data (Section 2.2.1.3).

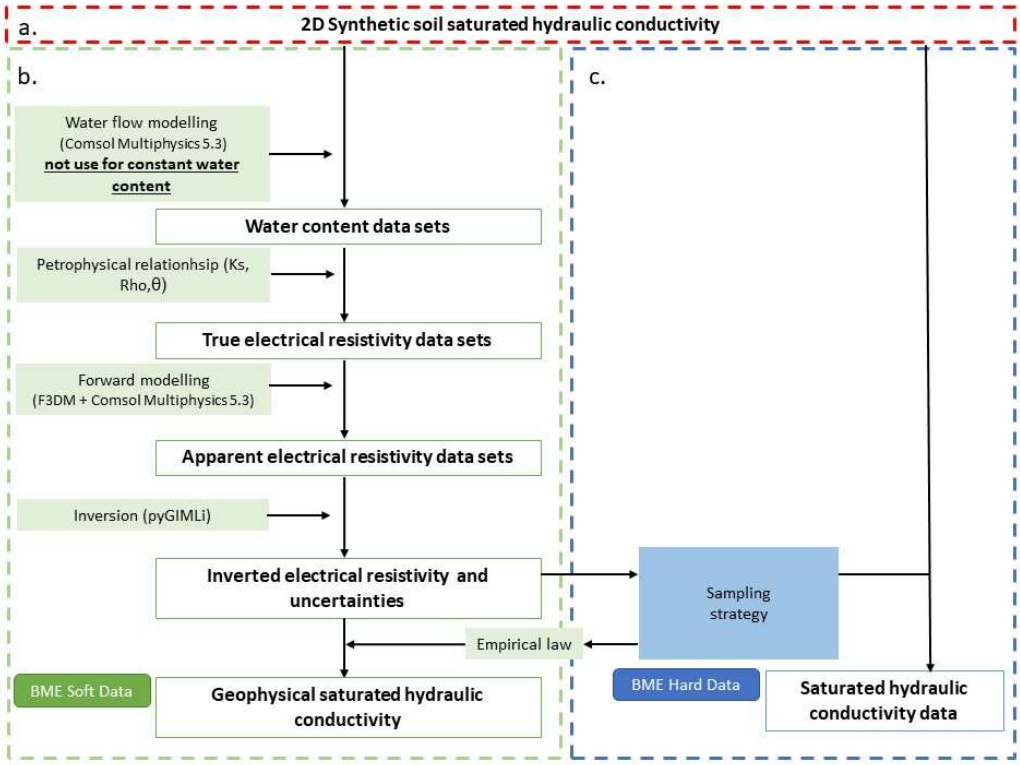

Figure 1: Schematic diagram for generating synthetic datasets. In green: soft data represent spatial geophysical measurements; in blue: hard data correspond to infiltration tests (Ks measurement).

2.2.1.1. Ks reference models

Figure 2a presents three different Ks_{ref}. We have chosen to show Ks_{ref} anomalies with a metric horizontal extension. In the BME framework, all data are introduced in $\log_{10}$ for purposes of

computation. The 3 models of $\log_{10}(Ks_{ref})$ have been grouped in Figure 2a. These three models have been chosen based on various criteria. The first model is a field case presented in an article (Bisone *et al.*, 2017a) devoted to a study of an infiltration site. The two other geological configurations are known to be difficult to reconstruct using ERT (Telford *et al.*, 1990).

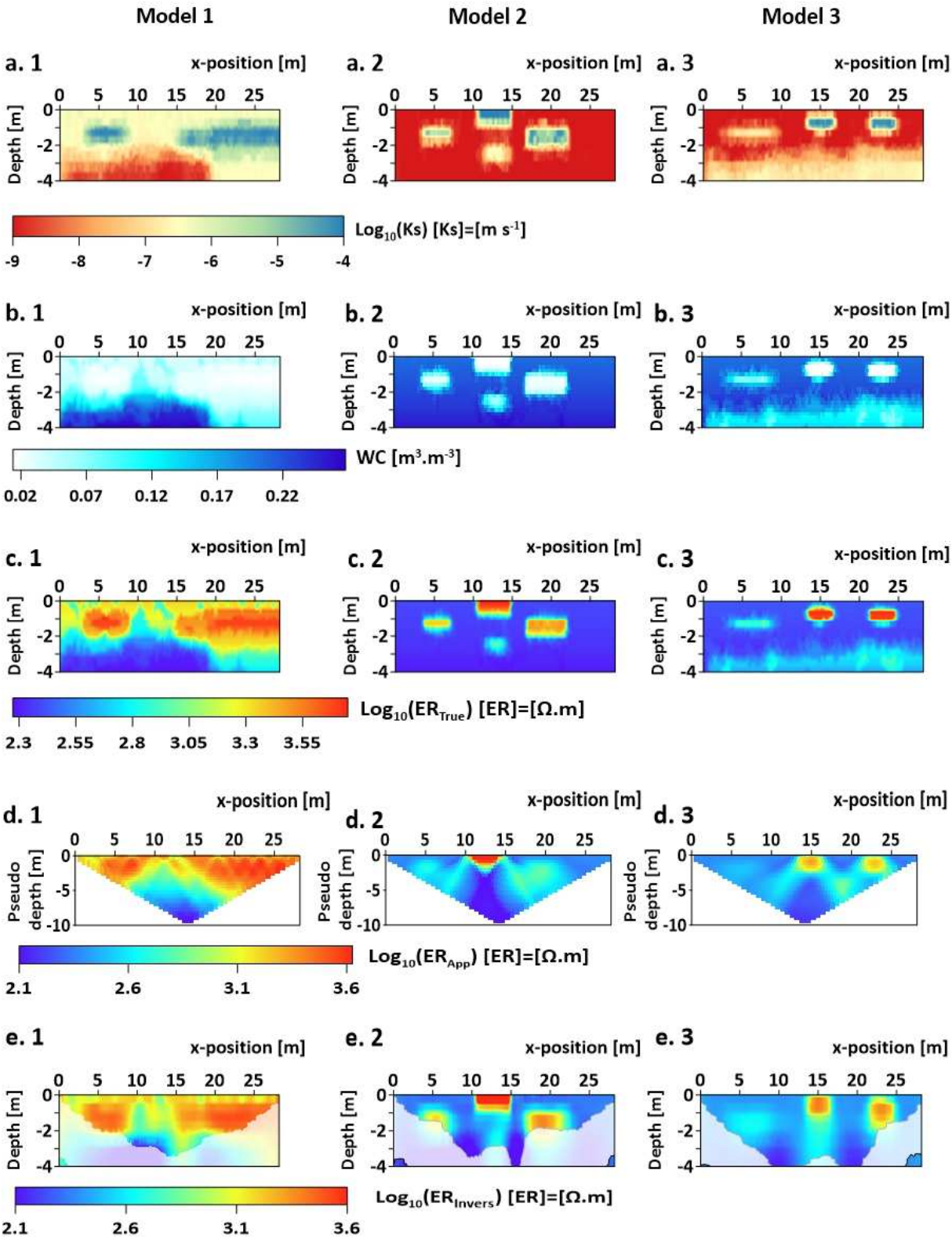

Figure 2: Three synthetic datasets: a) $log_{10}(Ks_{ref})$, b) WC, c) $log_{10}(ER_{True})$, d) $log_{10}(ER_{App})$, and e) $log_{10}(ER_{Interp})$

2.2.1.2. Soft data generation

2.2.1.2.1. Subsurface flow modeling: Water content estimation

According to Figure 1b, the first soft data generation step calls for WC simulation using subsurface flow modeling for variably-saturated soils. As suggested in Audebert *et al.* (2016), we will employ a single continuum model based on Richard's Equation (Richards, 1931), as completed with Mualem-van Genuchten's retention model, which expresses the relationship between water pressure and effective saturation (retention properties) as well as between relative Ks and effective saturation. To simulate TWW subsurface flow, we ran Comsol Multiphysics 5.4 with a subsurface flow module. The study domain is a 2D vertical profile 29.2 m long and 6 m high. The water flow boundary conditions were set as follows: (i) "No flow" on the top and sides; and (ii) "seepage face" for the bottom, as in Audebert *et al.* (2016). To assign all hydraulic parameters, we extracted from the literature 12 soil types with known parameters. Considering $\log_{10}(Ks_{ref})$, for each cell in Table 1, we sought the Ks corresponding to the closest Ks_{ref} value and assigned the remaining hydraulic parameters (Θs, α and n).

Table 1: Mualem - van Genuchten parameters and saturated hydraulic conductivity (Ks) of soil derived from Rosetta (Schaap *et al.*, 2001)

Textural class	Mualem-van Genuchten hydraulic parameters			
	Θs [$L^3.L^{-3}$]	α [m^{-1}]	n [-]	log_{10}(Ks) [Ks]=[$m.s^{-1}$]
Coarse sand	*0.33*	*7.44*	*2.96*	*-3.48*
Sand	*0.43*	*14.5*	*2.68*	*-6.08*
Loamy Sand	*0.41*	*12.4*	*2.28*	*-6.39*
Sandy Loam	*0.41*	*7.5*	*1.89*	*-6.91*
Loam	*0.43*	*3.6*	*1.56*	*-7.47*
Silt	*0.46*	*1.6*	*1.37*	*-8.16*
Silty Loam	*0.45*	*2*	*1.41*	*-7.90*
Sandy Clay Loam	*0.43*	*14.5*	*2.68*	*-6.08*
Clay Loam	*0.41*	*1.9*	*1.31*	*-8.14*
Silty Clay Loam	*0.43*	*1*	*1.23*	*-8.71*
Sandy Clay	*0.38*	*2.71*	*1.23*	*-8.48*
Silty Clay	*0.36*	*0.5*	*1.09*	*-9.26*
Clay	*0.38*	*0.8*	*1.09*	*-8.26*

To simulate variably-saturated soil, the model was initiated with a saturation set to 1. During a requisite time interval, the model was left to simulate soil drainage until the water table was close to 4 m deep. This value was chosen so that the given configuration could be considered free of any water table influence on the infiltration test within the first 2 m of soil. This set-up produced variable 2D-WC maps; for the constant WC model, we simply chose a value of 0.25 $m^3.m^{-3}$.

2.2.1.2.2. Petrophysical relationship

Just a few articles in the literature include the petrophysical relationship in determining Ks with the true electrical resistivity of soil ($\mathrm{ER_{True}}$) (Vogelgesang *et al.*, 2020). Soil WC can be considered as the most influential parameter on $\mathrm{ER_{True}}$; it is necessary therefore to take the variability of WC and Ks into account in the relationship. According to the literature, potential physical relationships between ER and WC are specific to a given soil type (Brunet *et al.*, 2010). For this study, we extracted the (WC, ER) pairs measured in the laboratory for broad sandy, loamy and clayey soil textures (Wunderlich *et al.*, 2013) and associated a $log_{10}(Ks)$ value with each relationship (Mallants *et al.*, 2003). A 2D interpolated map of $\mathrm{ER_{True}}$ was estimated as a function of Ks and WC (Figure 3). Based on both the

WC model and $log_{10}(Ks)$ reference model, for each cell estimating $log_{10}(ER)$, the closest WC and $log_{10}(Ks)$ values were sought (Figure 2c).

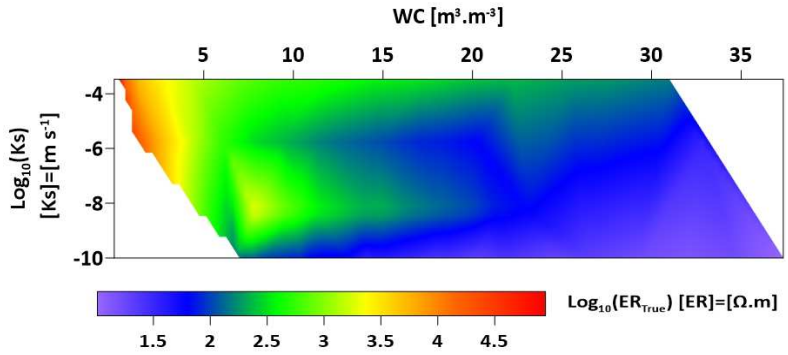

Figure 3: Results of the interpolation of $log_{10}(ER_{True})$ vs. WC and $log_{10}(Ks)$

2.2.1.2.3. Electrical resistivity tomography

The ERT measurement has been well described in the geophysical literature (Clement *et al*., 2020). $\mathrm{ER_{App}}$ is measured by injecting electric current into the ground with two current electrodes, in measuring the potential difference between two other electrodes; this device is called a quadrupole. The distribution of ER in the soil is determined by operating many quadrupoles at various positions along a line of electrodes installed at the surface of the soil. At the end of the measurement sequence, all quadrupoles are inverted using an inversion code (Telford *et al*., 1990).

2.2.1.2.3.1. Forward modeling

To simulate $\mathrm{ER_{App}}$ on each of the three synthetic ER models (Figure 2c), we ran the Comsol Multiphysics and Matlab F3DM 3.08 package, which is commonly used in geophysics forward modeling with the AC/DC module (quasi-stationary electromagnetic field in accordance with electromagnetic field theory) to evaluate the potential difference induced by the injected current (Clement and Moreau, 2016). A Gaussian noise distribution with a 3% standard deviation relative error was added to the $\mathrm{ER_{App}}$ dataset to simulate the noise commonly recorded in the field (Friedel, 2003). An acquisition line of 72 electrodes was implemented at a 0.4-m spacing. A complete sequence of 829 quadrupoles was carried out with Wenner Arrays.

2.2.1.2.3.2. Inversion procedure

The synthetic $\mathrm{ER_{App}}$ was inverted using pyGIMLi, an open-source multi-method library for geophysics modeling and inversion (Rücker *et al.*, 2017). A finite element method, relying on regular grid models, was applied to solve the forward problem in the routine inversion program. An isotropic smoothness-constrained regularization and a quasi-Gauss Newton optimization method were both used along with a fixed regularization parameter (λ= 30, $\mathrm{Zweight} = 1.0$). This inversion procedure produced an $\mathrm{ER_{Interp}}$ map (Günther and Rücker, 2011).

2.2.1.2.3.3. Uncertainties

An interpreted ERT is not the perfect image of $\mathrm{ER_{True}}$. The smooth nature of electrical current implies a loss of resolution when moving away from the electrodes. In some parts of the inverted model, the ER value of a cell has a very low impact on the measured $\mathrm{ER_{App}}$. It is therefore of paramount importance to account for the uncertainty on ERT.

The total uncertainty of ER depends on: the inversion process, the measured data, and the loss of information with depth. Calculating total uncertainty is a long and complex process; consequently, it is proposed herein to estimate uncertainty by means of simple inversion indicators derived from the geophysical literature, namely: coverage, resolution radius (Friedel, 2003), or DOI (D. Carrière *et al.*, 2014). All inversion indicator calculations require knowledge of the Fréchet derivative matrix G[N×M], also called the Jacobian matrix or sensitivity matrix (Equation 1):

$$\mathrm{G_{i,j}} = \frac{\partial \mathrm{d_i}}{\partial \mathrm{m_j}} \quad \mathrm{i} = [1\colon \mathrm{N}],\ \mathrm{j} = [1\colon \mathrm{M}] \qquad \textit{Equation 1}$$

where $\mathrm{d_i}$ and $\mathrm{m_j}$ are the $\mathrm{ER_{App}}$ data and model parameter, respectively. A single sensitivity value $\mathrm{G_{i,j}}$ indicates the change in apparent resistivity data $\mathrm{d_i}$ m with respect to a small change in model parameter $\mathrm{m_j}$. G is used to determine how a change in resistivity of model cell j affects the measured value of $\mathrm{d_i}$. In our case, we have opted for model resolution $\mathrm{R_M}$, where the $\mathrm{R_M}$ matrix is calculated by inversion software according to the following formula (Equation 2) (Günther, 2004):

$$\mathrm{R_M} = \left(\mathrm{G^T W_d^T W_d G} + \lambda \mathrm{C^T C}\right)^{-1} \mathrm{G^T W_d^T W_d G} \qquad \textit{Equation 2}$$

where G is the sensitivity matrix, W_d a diagonal matrix containing the data errors, λ the damping parameter, and C the *a priori* model covariance matrix. The diagonal element R_{ii} indicates how the inverted model of ER is resolved. If all diagonal elements of R_M equal 1, then the "exact model" is perfectly resolved. The further the R_M diagonal element from 1, the poorer the resolution. In accordance with the ideas of (Friedel, 2003), a resolution radius for each model cell can be determined from the diagonal elements of the resolution matrix R_{ii}. Let's assume a piecewise constant cell resolution with r_{les}^{i} as the radius of a cell circle having a perfect resolution of 1. For a cell of dimensions Δx_i and $I\Delta z_i$, the resolution radius is defined by Equation 3 below:

$$r_{Res}^{i} = \sqrt{\frac{\Delta x_i \Delta z_i}{\pi R_{ii}}} \qquad \textit{Equation 3}$$

The resolution matrix r_{Res} allows assessing the reliability of the inverted models according to the degree of resolution specific to each cell. r_{Res} is therefore the most suitable indicator for unstructured or irregular BERT meshes. For this reason, r_{Res} has been chosen as an uncertainty to be introduced into the BME (Section 2.3).

2.2.1.3. Hard data generation: Hydraulic conductivity sampling method

We have sampled hard data $log_{10}(Ks_H)$ by extracting the $log_{10}(Ks)$ value from $log_{10}(Ks_{ref})$ (Figure 2a). It is assumed that our measurements of $log_{10}(Ks_H)$ have a zero variance. We used ER_{Interp} data and a random selection technique to optimize the Ks sample location, as per the following strategy:

- 50% of the number of points were manually sampled above and below the anomalies.
- 25% of the points were sampled in the upper part of the ER_{Interp} map, where R_{res} has low uncertainty. Our ER_{Interp} maps were divided into three ranges, between the min and max values. In each range, an equivalent number of points were randomly sampled.
- 25% were sampled in the area with the lowest r_{Res}; these points were sampled entirely randomly, owing to the poor performance of ERT in this area.

For this step, the spatialization of Ks with the BME has been tested with three differing sample numbers, i.e. 14, 24 and 50.

2.2.2. Field data

The experimental site is located in France and had already been studied in previous articles (Benz-Navarrete *et al.*, 2019). It comprises a fairly heterogeneous agricultural plot and is relatively tabular in its sandy-loam surface, presenting sandy lenses in loam over its depth. ERT acquisitions were carried out using Iris Instruments' "Syscal Pro 72-electrodes" resistivity-meter (IRIS Instruments, France). The ERT profile was acquired with a Wenner array-type and a 0.25-m electrode spacing. To cover the proposed profile length (45 m) and maintain reasonable subsurface lateral resolution, the roll-along acquisition technique was performed with 48 electrode overlaps. The contact resistance was continuously measured at less than 4 kOhms. The 2D image of the $\mathrm{ER}_{\mathrm{Interp}}$ profile was inverted with the pyGIMLi software (Rücker *et al.*, 2017); a 2D flat inversion was carried out. We chose an isotropic smoothness constraint, with a Z-weight of 1 and a lambda value of 30 (Günther, 2004; Loke, 1999). Moreover, we used a tetrahedral mesh with 2,920 cells.

According to the sampling strategy presented in the previous section, 23 infiltration test locations were selected. The Aardvark permeameter, developed by Soil Moisture Inc. (USA), was employed to measure the infiltration rate. From the measured flow rate, $\log_{10}$(Ks) could be estimated by applying Reynolds and Elrick's equation (Elrick *et al.*, 1989).

2.3. BME fusion method

The Bayesian Maximum Entropy (BME) method and its BMElib numerical implementation (Christakos *et al.*, 2002; Serre and Christakos, 1999) provide a mathematically rigorous framework that incorporates information from several data sources featuring different uncertainties and point densities. These data have been organized into both "hard data" corresponding to exact measurements and "soft data" with a given uncertainty.

The spatial random field Y(x,z)=$\log_{10}(\mathrm{K_S}(x,z))$ indicates $\log_{10}(\mathrm{K_S})$ of the soil at location (x,z), where x (m) is the longitudinal coordinate along our study transect, and z (m) the depth. $\mathrm{Y_h}$, $\mathrm{Y_s}$ and $\mathrm{Y_k}$ denote Y at: the hard data points (where $\mathrm{Y_h}$ is obtained from geotechnical measurements), the soft data points (where $\mathrm{Y_s}$ is derived from ERT and petrophysical relationships), and the estimation point, respectively.

BME relies on two principles: (i) maximum entropy theory processes the general knowledge base of means and covariances $\mathrm{G}=\{\mathrm{m_Y},\mathrm{cov_Y}\}$ and produces a "prior" $\mathrm{f_G}$ PDF (probability density function) describing the spatial process; and (ii) Epistemic Bayesian conditioning updates this prior $\mathrm{f_G}$ PDF with the site-specific knowledge base S, which then yields a BME posterior PDF $\mathrm{f_k}$ describing the value $\mathrm{Y_k}$ at any estimation point. Here, $\mathrm{S}=\{\mathrm{Y_h},\mathrm{f_S}\}$, where $\mathrm{Y_h}=\log_{10}(\mathrm{Ks}_H(x,z))$ is the measurement of the hard geotechnical data and $\mathrm{f_S}$ is a PDF describing the uncertainty associated with soft geophysical data; moreover, the BME posterior PDF is given by:

$$\mathrm{f_k}(\mathrm{Y_k})=\mathrm{A}\int \mathrm{f_G}(\mathrm{Y_h},\mathrm{Y_S},\mathrm{Y_k})\mathrm{f_S}(\mathrm{Y_s})\mathrm{dY_s}, \qquad \text{Equation 4}$$

where A is a normalization constant.

The mean $\mathrm{m_Y}$ of field Y(x,z) is set to a first-degree polynomial, while the covariance $\mathrm{cov_Y}$ is obtained by fitting an anisotropic covariance model to experimental covariance values calculated from the $\mathrm{Y_h}$ data. A covariance model quantifies the degree of similarity between pairs of measurements in terms of their separation distance and the orientation of the line between such pairs. See Chils and Delfiner (1999) for details on how covariance models describe the variability of spatial processes; also, Olea (2006) provided details on fitting a covariance model to experimental covariance values obtained from a covariogram analysis. In this study, the experimental covariance values are calculated based on a sample size (of $\mathrm{Y_h}$ measurements). The anisotropy model fitted to these experimental covariance values is assumed to be exponential, with a major direction aligned with the x (longitudinal) axis, and a ratio of covariance ranging along the major direction over the covariance ranging along the transverse direction.

The soft data PDF $f_S(Y_s)$ is obtained by transforming $\log_{10}(ER_{Interp})$ into $\log_{10}(Ks_{Geo})$. (Mastrocicco et al., 2010) proposed a log-linear relationship between ER and Ks, hence the need for a linear regression of the observed $\log_{10}(Ks_{Geo})$ with respect to their corresponding $\log_{10}(ER_{Interp})$. Then, for each node of the inversion grid where a $\log_{10}(ER_{Interp})$ is available but for which $\log_{10}(Ks_H)$ was not measured, we set $f_S(Y_s)$ to a Gaussian PDF with a mean equal to the value predicted by linear regression $Y_s = \log_{10}(Ks_{Geo})$. However, for BME to work efficiently, we must set the variance $\sigma_s^2(x,z)$ of $f_S(Y_s)$ to a value that captures the uncertainty in the Y_s obtained from $\log_{10}(ER_{Interp})$ at location (x,z). This can be accomplished by using the following:

$$\sigma_s^2(x,z) = \frac{r_{res}(x,z)}{mean(r_{res})}\sigma_{Y_h}^2 + \frac{|z|}{mean(|z|)}\sigma_z^2 \qquad \textit{Equation 5}$$

where $r_{res}(x,z)$ is the resolution radius (Section 2.2.1.2.3.3), mean($r_{res}(x,z)$) its mean, $\sigma_{Y_h}^2$ the variance of Y_h, $|z|$ the absolute value of depth, $mean(|z|)$ its mean, and σ_z^2 a parameter obtained by maximizing the R^2 of validation (as explained in previous section). The terms $\frac{r_{res}(x,z)}{mean(r_{res})}$ and $\frac{|z|}{mean(|z|)}$ are unitless, while both $\sigma_{Y_h}^2$ and σ_z^2 have units of $\log_{10}(m.s^{-1})^2$. The first term in Equation 5 is equal to the resolution radius normalized to a variance, while the second term is a gradient with depth, also normalized to a variance. Combined, these two terms allow the BME to account for the fact that the uncertainty in the soft geophysical data increases with both r_{res} and depth.

2.4 BME validation strategy

We adopted a validation strategy to compare the estimation error of three methods: kriging (of the hard data alone), geophysics (i.e. geophysical data alone), and BME (i.e. fusion of both hard data and geophysical data). For the numerical simulations, we computed the estimation error by comparing the estimated Ks with $\log_{10}(Ks_{ref})$. Our field study was limited to $\log_{10}(Ks_H)$ at nh sampled locations, in which case we conducted a cross-validation analysis (Lee et al., 2009). The validation statistics used to assess model performance were: mean square estimation error (MSE), mean

293 estimation error (ME), variance of estimation error (VE), and square of the Pearson correlation
294 coefficient R^2 (Christensen, 2018).

295 # 3. Results

296 ## 3.1. Numerical approach

297 ### 3.1.1. Evaluation of hard data number

298 Figures 4, 5 and 6 show the spatial distribution of $\log_{10}(\mathrm{Ks})$ for synthetic models 1, 2 and 3,
299 respectively. The three columns in each figure represent the spatialization result when the number of
300 sampling points where $log_{10}[Ks_H]$ has been sampled equals 10, 24 and 50, respectively. The rows
301 offer the following:

302 - Row 1: $\log_{10}(\mathrm{Ks}_{\mathrm{ref}})$.
303 - Row 2: $\log_{10}(\mathrm{ER}_{\mathrm{Invers}})$ data. The black circles indicate the sampling locations (where the
304 $log_{10}(Ks_H)$ data has been sampled from $log_{10}(Ks_{ref})$).
305 - Row 3: $\log_{10}\mathrm{Ks}_{\mathrm{Geo}}$.
306 - Rows 4 and 5: results of the spatialization $\log_{10}(\mathrm{Ks}_{\mathrm{H}})$ data by means of kriging
307 $\log_{10}(\mathrm{Ks}_{\mathrm{Krig}})$, associated with variance map σ^2_{Krig}.
308 - Rows 6 and 7: $\log_{10}(\mathrm{Ks}_{\mathrm{BME}})$ and the estimated variance map σ^2_{BME}.

309 The columns in each figure present all the results for several Ks samples (nh). Tables 2, 3 and 4
310 respectively summarize the following statistical tools: MSE, ME, VE, and R^2, applied to evaluate the
311 performance of these estimation methods.

312 #### *3.1.1.1. Model 1*

313 Figure 4b.3 shows the $\log_{10}(\mathrm{ER}_{\mathrm{Interp}})$ map for a 50-point sampling (nh=50) conducted on a two-
314 layer soil. The surface displays an initial layer (depth: 0-2.5 m) with an estimated $\log_{10}(\mathrm{ER}_{\mathrm{Interp}})$ of
315 1.8. Two anomalies are present in this layer, at x = 5 m and 22 m. The synthetic reference model
316 (Figure 4a) shows two anomalies with the same thickness, whereas the anomalies are deformed and
317 stretched downward in Figure 4b. At depth, the layer with $\log_{10}(\mathrm{ER}_{\mathrm{Interp}})$ of 1.4 is more reduced

than that in the reference model; it starts at the x = 2.5 m position and disappears at the x = 17 m position. In Figure 4c.3, the $\log_{10}(\mathrm{Ks}_{\mathrm{Geo}})$ distribution is very similar to the $\log_{10}(\mathrm{ER}_{\mathrm{Interp}})$ map. In Figure 4d.3, the result of kriging based solely on $\log_{10}(\mathrm{Ks}_{\mathrm{H}})$ reveals a highly smoothed map; however, the BME results lie closest to the reference model. The surface anomalies are in the correct position and the shape of the anomaly is closer to reality (Figure 4f.3).

Reducing the number of samples to 24 hard data ($\log_{10}(\mathrm{Ks}_{\mathrm{H}})$) produces no noticeable change in the proposed $\log_{10}(\mathrm{Ks}_{\mathrm{Geo}})$) map. Kriging is more likely to overwhelm the anomalies. The BME fusion method provides an attractive $\log_{10}(\mathrm{Ks}_{\mathrm{BME}})$ estimate, with a reasonable number of samples. Let's note that reducing the number of points at depth reduces resolution of the anomaly at the position x = 10 m and z = 3.5 m.

The 14 sampling points are insufficient to cover all anomalies, which obviously influences the kriging results and geophysical transformation by the empirical law; therefore, the BME fusion method is closest to the reference model. Indeed, the BME is capable of delineating large sand anomalies, yet it tends to underestimate the extent of the clay anomaly at depth. This finding can be explained by the lack of resolution of the ERT method at depth, where information from soft data is less reliable. Figures 4e and 4g exhibit the variance for both the kriging and BME methods. The information given by the σ^2_{Krig} map is weak for data close to the Ks hard value: σ^2_{BME} is minimized compared to σ^2_{Krig}. All visual results have been confirmed by error estimators, which are more efficient for the BME.

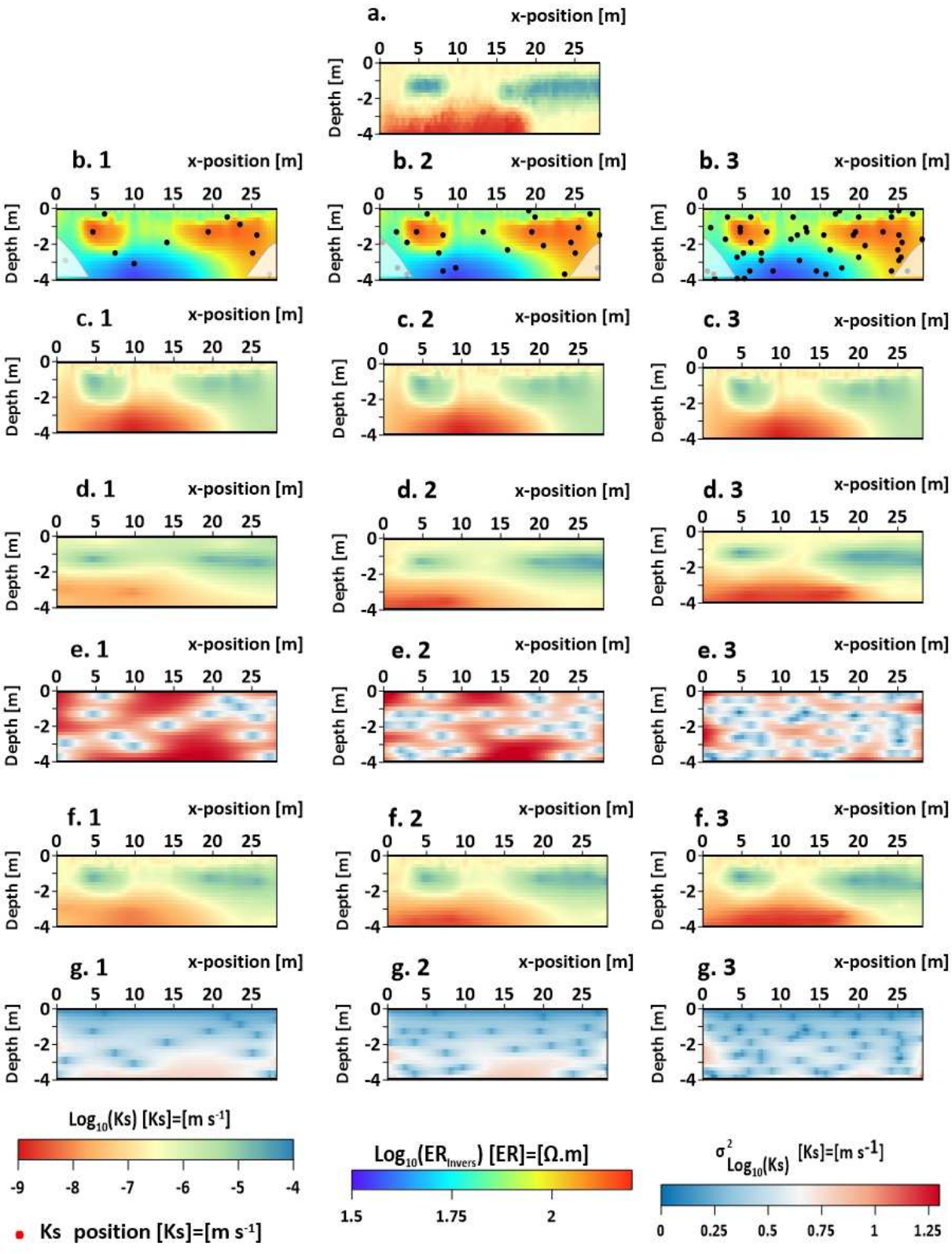

Figure 4: Spatial estimation of $log_{10}(Ks)$ and its variances for Model 1: kriging, geophysical transformation and BME at a constant WC for 14, 24 and 50-point sampling

340 *Table 2: Statistical analysis of the spatialization of Model 1 for the three samples*

		Model-1			
Method	nh	MSE	ME	VE	R^2
Kriging	14	0.44	0.28	0.36	0.76
Geophysics		0.23	0.02	0.23	0.83
BME		0.23	0.11	0.22	0.88
Kriging	24	0.27	0.13	0.25	0.83
Geophysics		0.23	0.08	0.23	0.83
BME		0.18	0.09	0.17	0.89
Kriging	50	0.12	0.00	0.12	0.91
Geophysics		0.24	-0.04	0.24	0.83
BME		0.11	-0.03	0.11	0.92

341

342 #### *3.1.1.2. Model 2*

343 Figure 5 shows the spatialization of $\log_{10}(\mathrm{Ks})$. Figure 5b.3 presents the $\log_{10}(\mathrm{ER}_{\mathrm{Interp}})$ map and
344 estimated $\log_{10}[\mathrm{Ks}_{\mathrm{H}}]$ for 50 sampling points. In Figure 5c.3, $\log_{10}(\mathrm{Ks}_{\mathrm{Geo}})$ reveals the three clay
345 anomalies on the surface, but the silty anomaly is not apparent. The clay anomalies are stretched
346 towards the bottom. In Figure 5d.3, kriging serves to identify the four anomalies; however, even with
347 such a large sample, kriging merges the two near-surface anomalies at the position x = 16 m. In
348 Figure 5f.3, the anomalies are correctly delineated with BME. We can observe that kriging
349 deteriorates and merges the anomalies. BME would appear to be better with 24 points than with 50
350 because the loam anomaly is more sharply defined with 24 points. In reality, this outcome is due to
351 the differentiation in the selected sampling points. More specifically, with a minimal number of 14 Ks
352 hard data, results maintain the same trend as with 50 and 24 points. Table 3 shows that for 50
353 $\log_{10}(\mathrm{Ks}_H)$ sampling points, the BME method slightly improves the estimation result in terms of
354 correlation (R^2=0.82 for nh=14 vs. R^2=0.84 for nh=50) and targeting (MSE around 0.3). The increase in
355 number of samples (from 14 to 24 points) degrades the kriging estimate in terms of correlation; this
356 trend is linked to the random sampling that in this case has selected points of lesser interest.

Regardless of the number of samples, the R^2 calculation demonstrates that BME once again produces the highest value in this second model.

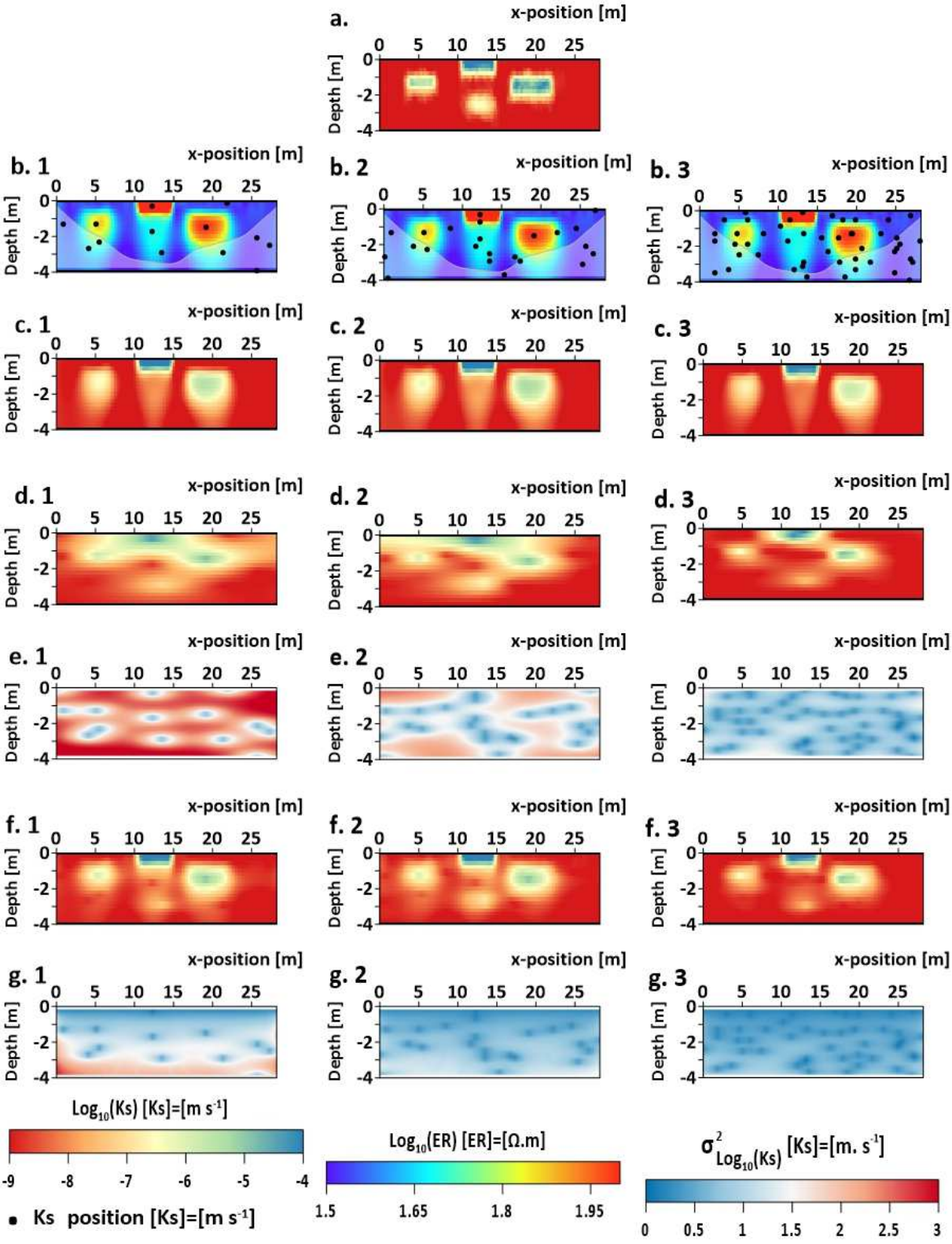

Figure 5: 2D estimation of $log_{10}(Ks)$ and variances for Model 2: kriging, geophysical transformation and BME at a constant WC for 14, 24 and 50-point sampling

Table 3: Statistical analysis of the spatialization of Model 2 for the three samples

		Model-2			
Method	nh	MSE	ME	VE	R^2
Kriging	14	1.52	0.75	0.97	0.43
Geophysics		0.41	0.07	0.41	0.75
BME		0.36	0.26	0.29	0.82
Kriging	24	1.46	0.57	1.14	0.39
Geophysics		0.45	0.22	0.41	0.75
BME		0.36	0.27	0.29	0.82
Kriging	50	0.51	0.03	0.51	0.69
Geophysics		0.40	-0.07	0.40	0.75
BME		0.28	-0.05	0.28	0.84

3.1.1.3. Model 3

Figure 6 presents the results of the spatialization of $\log_{10}(Ks)$. For 50 points (Figure 6b.3), $\log_{10}(\mathrm{ER}_{\mathrm{Interp}})$ indicates the presence of two sand anomalies with a $\log_{10}(\mathrm{ER}_{\mathrm{Interp}})$ of 2 and one loam anomaly with a $\log_{10}(\mathrm{ER}_{\mathrm{Interp}})$ of 1.7; meanwhile, ERT does not show the deep clay layer. In Figure 6c.3, $\log_{10}(\mathrm{Ks}_{\mathrm{Geo}})$ follows the $\log_{10}(\mathrm{ER}_{\mathrm{Interp}})$ map. The kriging result in Figure 6d.3 exposes a deep loam layer with well delimited anomalies. At the surface however, the method tends to merge anomalies. The BME results in Figure 6f.3 clearly identify the 3 anomalies as well as the loamy layer. With 24 points, kriging (Figure 6d.2) of the surface anomaly is merged. The near-surface anomalies and deep layer are well distinguished in Figure 6g.2 with BME methods; however, the first anomaly on the left has been attenuated. With 14 points, BME correctly reproduced (Figure 6g.1) the near-surface anomalies except for the loamy layer at depth. Visually, the BME method produces the best results.

Table 4 of the statistical indicators confirms that BME is, regardless of the number of points, always higher than kriging or geophysical transformation. In conclusion, the BME method seems to extract the best information from geophysical transformation and kriging; however, the number of samples does influence the spatialization of Ks by BME. In taking the results and statistical analysis into account, we feel that 20 infiltration test points offers a valuable number of points.

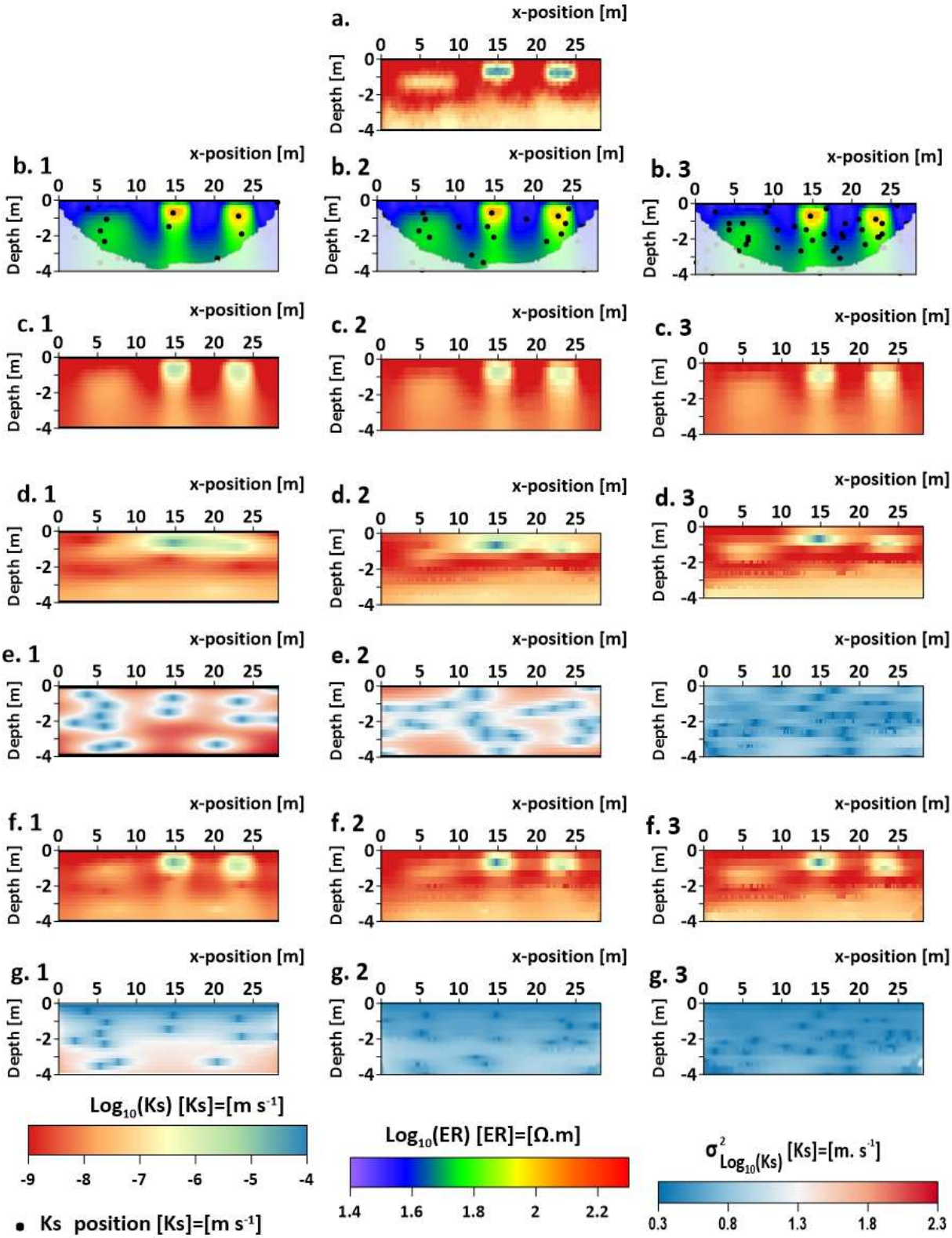

382

383 *Figure 6: Spatialization of $log_{10}(Ks)$ for Model 3: kriging, geophysical transformation and BME*

384 *at a constant WC for 14, 24 and 50-point sampling*

385

Table 4: Statistical analysis of the spatialization of Model 3 for the three samples (14, 24 and 50)

		Model-3			
Method	nh	MSE	ME	VE	R^2
Kriging	14	1.13	0.33	1.02	0.23
Geophysics		0.83	-0.37	0.69	0.43
BME		0.44	-0.13	0.43	0.68
Kriging	24	0.85	0.21	0.81	0.36
Geophysics		0.79	-0.32	0.69	0.43
BME		0.33	-0.11	0.32	0.81
Kriging	50	0.37	0.02	0.37	0.71
Geophysics		0.76	-0.24	0.71	0.43
BME		0.29	-0.08	0.28	0.83

3.1.2. Influence of variable soil WC

This section will consider the influence of variable soil WC, with 24 hard data values and the three same $\log_{10}(\mathrm{Ks}_{\mathrm{ref}})$ models. All results are presented in Figure 7; each column of the figure lists all results for the various models.

Figure 7b displays $\log_{10}(\mathrm{ER}_{\mathrm{Interp}})$, which has decreased in depth and increased at the surface. This change can be explained by the variable WC obtained from the groundwater flow model. Model 1 in Figure 7 shows that the simple petrophysical transformation of the data does not highlight the variations in $\log_{10}(\mathrm{Ks})$. Let's also note that the anomalies are heavily distorted, along with the presence of an artifact at the 15-m position of the clay anomaly at depth. For Model 2, four anomalies are distinguished, though a deep stretching of the central anomaly can be observed (Figure 7c.2). Model 3 exhibits the three anomalies, but the clay layer is poorly defined; the loamy layer ($\log_{10}(Ks_{ref})$=-7) (Figure 7a.3) at depth has been replaced by a clay layer ($\log_{10}(Ks_{Geo})$=-9) (Figure 7c.3).

The BME method is the one that best estimates the $\log_{10}(\mathrm{Ks})$ data. Compared to the reference models, the BME spatialization ($\log_{10}(Ks_{BME})$) actually reproduces all anomalies of the three distinct models.

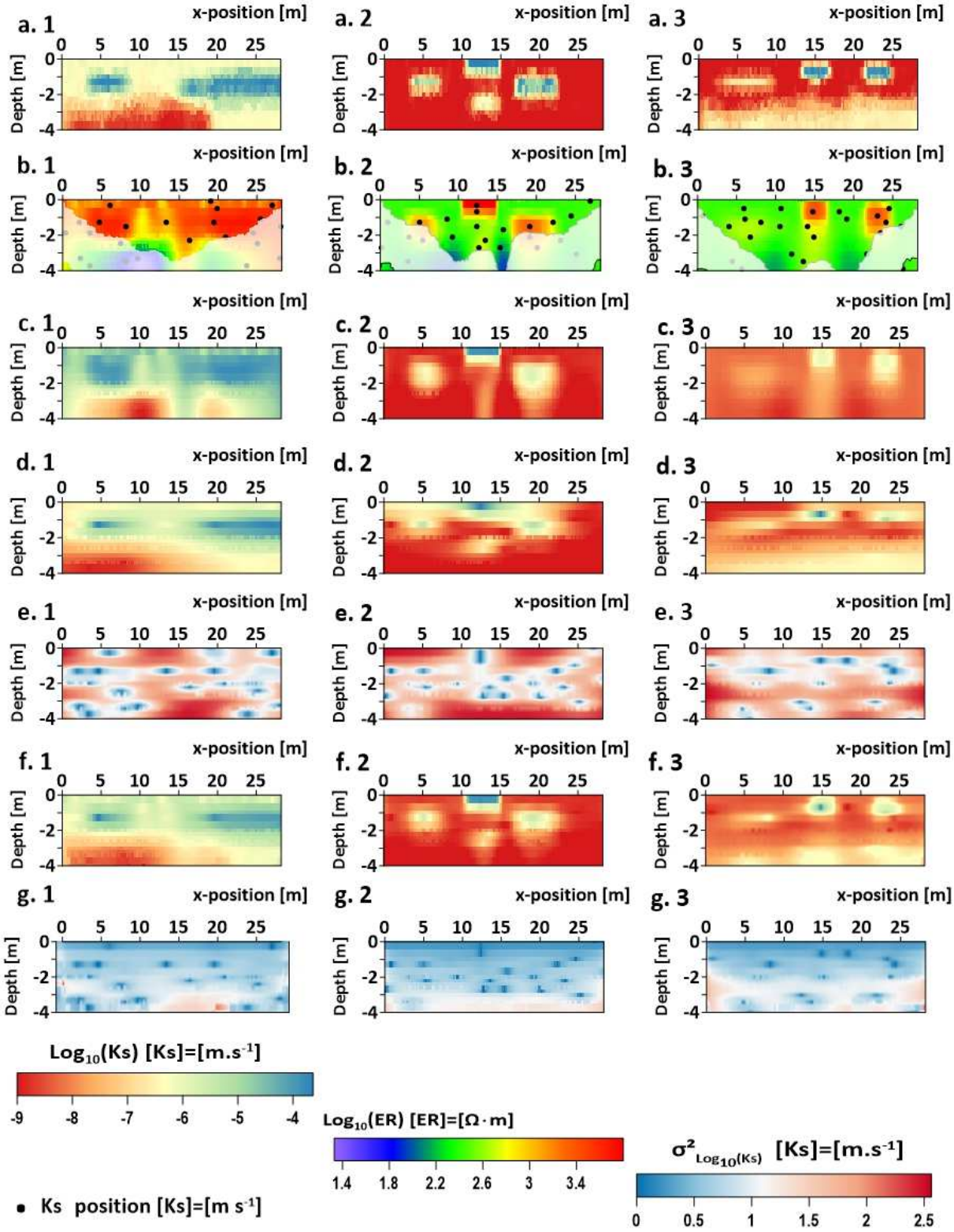

404

405 *Figure 7: Spatialization of $log_{10}(Ks)$ for Models 1, 2 and 3: kriging, geophysical transformation*

406 *and BME at a variable WC for 24-point sampling*

407

Table 5: Statistical analysis of spatialization with BME, kriging and petrophysical relationship for all three models

Method	Model	MSE	ME	VE	R^2
Kriging	1	0.28	0.14	0.26	0.81
Geophysics		0.46	0.10	0.45	0.68
BME		0.29	0.16	0.26	0.82
Kriging	2	1.23	0.38	1.08	0.41
Geophysics		0.48	0.06	0.48	0.70
BME		0.33	0.10	0.32	0.80
Kriging	3	0.42	0.12	0.41	0.66
Geophysics		1.14	-0.14	1.12	0.08
BME		0.43	0.05	0.43	0.77

Table 5 reports on the statistical tools used to evaluate the performance of estimators (kriging, geophysics, BME) for all three models. It can be observed that the statistical analysis applied to the models studied shows a strong correlation between the reference model and the BME method result. For example, on Model 3, the correlation coefficient R^2 equals 0.77 for the BME vs. 0.66 for kriging or 0.08 for kriging geophysics. The lower MSE value obtained with BME (0.43) reflects BME's high accuracy and targeting. Although data from the $\log_{10}(\mathrm{ER}_{\mathrm{Interp}})$ map are degraded, this has nevertheless allowed BME to improve the Ks spatialization, an extremely encouraging result that underscores BME performance.

3.2. Field validation

Figure 8 presents the field result of a single ERT profile and 23 infiltration test $\log_{10}(\mathrm{Ks}_{\mathrm{H}})$ values. In Figure 8a, ERT results are presented on a 45-m line; also, the $\log_{10}(\mathrm{ER}_{\mathrm{Interp}})$ points of low sensitivity (coverage < 0.7) are masked. It can be acknowledged that the $\log_{10}(\mathrm{ER}_{\mathrm{Interp}})$ measurement in this area is not realistic. The $\log_{10}(\mathrm{ER}_{\mathrm{Interp}})$ data show variations from 1 to 2.2 ($\log_{10}(\Omega.\mathrm{m})$). Infiltration tests (as represented by black points) have allowed us to determine that the $\log_{10}(\mathrm{Ks}_H)$ of the parcel varies between -3 and -7 ($\log_{10}(\mathrm{m.s^{-1}})$); this value is standard for Limagne soils, which are often called "black soil". These soils contain varying clay and sand contents, which explains the $\log_{10}(\mathrm{Ks}_H)$ (Bornand *et al.*, 1984). The position of $\log_{10}(\mathrm{Ks}_H)$ was identified according to the

sampling strategy presented above. Figure 8c presents the mapping of $\log_{10}(\mathrm{Ks}_{\mathrm{Krig}})$ based solely on infiltration test data. Observations can be made of: a surface layer with an average value of -5 ($\log_{10}$(m.s^{-1})), a deep anomaly (at the position x = 20 m and y = -2 m) with a value of -6 ($\log_{10}$(m.s^{-1})), and another deep anomaly (at the position x = 4 m and y = -2 m) with a value of -3 ($\log_{10}$(m.s^{-1})).

Figure 8d provides the map of $\log_{10}(\mathrm{Ks}_{\mathrm{Geo}})$ from the petrophysical relationship. Let's note the various layers between 0 and -1 m, with values on the order of $\log_{10}\mathrm{Ks}_{\mathrm{Geo}}$=-4) ($\log_{10}$(m.s^{-1})). We can also distinguish a deep layer with values between -5 and -6 ($\log_{10}$(m.s^{-1})) inclusive. BME behaves here as the fusion of kriging and geophysical data. The surface layer is taken into account, and the deep anomalies highlighted by $\log_{10}(\mathrm{Ks}_{\mathrm{H}})$ appear in the final model of Ks. From a visual standpoint, BME takes the best features from both kriging and geophysics.

Based on cross-validation and statistical analysis (MSE, ME, VE and R^2), BME slightly improves results with a high R^2 correlation index of 0.78 and a low root mean square error of 0.46. According to our statistical analysis, the BME method proves to be the most highly focused, accurate and correlated method.

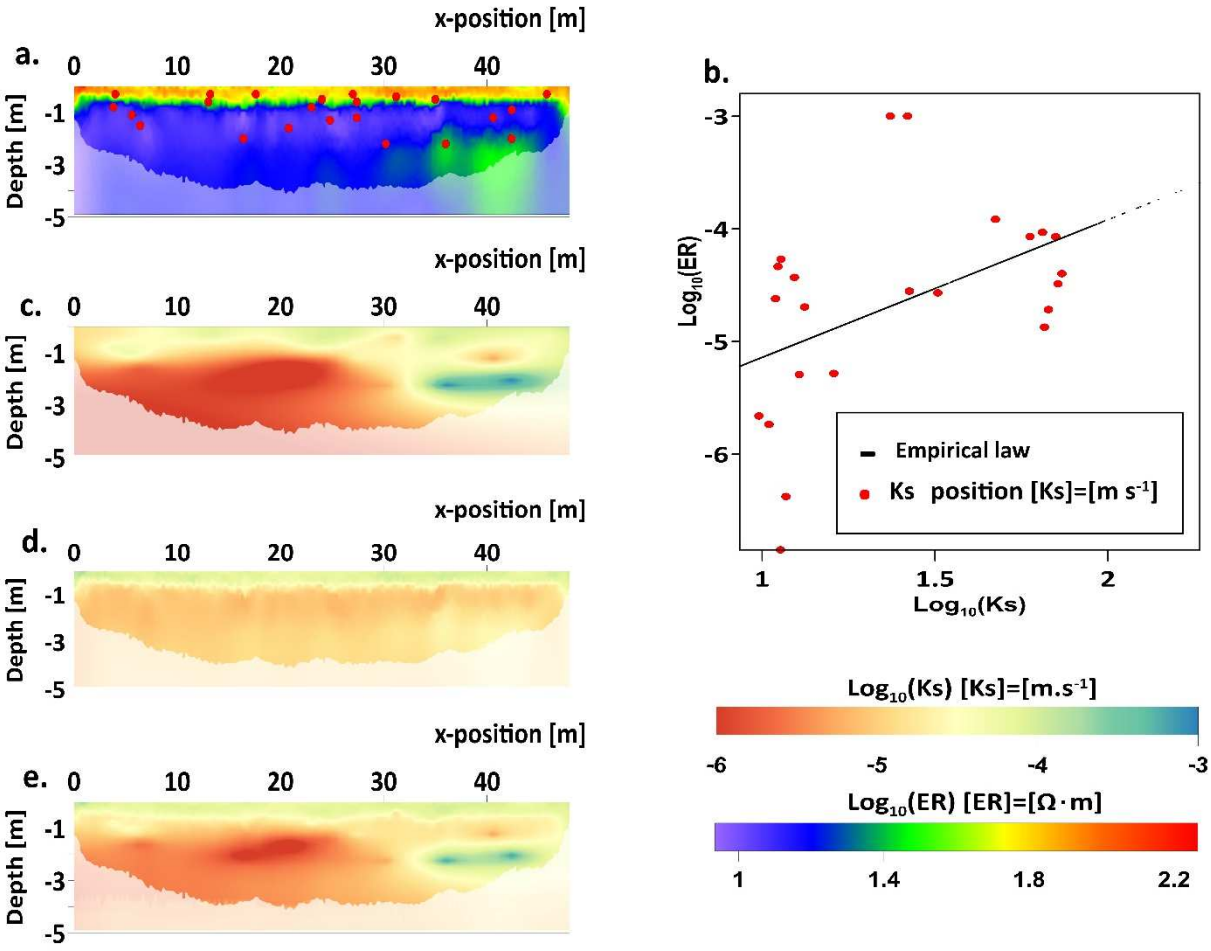

Figure 8: Spatialization of Ks on the data field: a) location map of infiltration tests on the $log_{10}(ER)$ profile (RMS = 3.55%); b) empirical law between $log_{10}(ER)$ and $log_{10}(Ks)$; c, d and e) Results of the spatialization of $log_{10}(Ks)$ by kriging, geophysics and BME, respectively

Table 6: Statistical analysis of the spatialization of Ks on field data

Method	MSE	ME	VE	R^2
Kriging	0.47	-0.08	0.49	0.77
Geophysics	0.51	-0.07	0.53	0.75
BME	0.46	-0.09	0.47	0.78

4. Discussion

Previous results lead the ensuing discussion to three points, namely: (i) the lack of validation data for BME generalization, (ii) the sampling strategy, and (iii) its future applications.

4.1. Lack of validation data

Due to the lack of validation data, it is extremely difficult to consolidate these approaches in the field. This work has proposed a static analysis to evaluate the BME data fusion methodology as a means of overcoming the absence of validation data. Nevertheless, the statistical indicator for 24 points is not adequately significant, and the method would require validation at other sites with a larger set of available Ks data. In spite of this fact, the method has allowed obtaining, for the very first time, an impressive map of Ks based on the available parcel information. To improve these BME methods in the future, an expanded number of measurements at well-known reference sites will be necessary. To date, the BME is an efficient method but cannot be definitively generalized.

4.2. Sampling strategy

The sampling strategy is based on ERT data for selecting the optimal Ks measurement location in the field. Such a strategy has proven to be successful but is still capable of being improved. Indeed, ERT does not recognize all potential anomalies. We have limited this bias by splitting our sampling strategy into two parts: first, sampling by electrical resistivity (ER) over a range with low uncertainty for the ERT measurements; then, sampling randomly where uncertainty is high. However, when using the numerical dataset, an evaluation of the hard data sampling number (Section 3.1.1.2) showed that 14 points could be better than 24 points for the kriging method, which means that the Ks sampling point location could be improved even further.

Sampling remains a highly critical issue, especially with such strong constraints on the number of Ks measurements; these constraints are time-consuming and therefore expensive. As a result, the number of tests should be minimized and optimally located when investigating a TWW infiltration area of use for the BME. This challenge still needs to be addressed in the future. The authors are convinced that a better sampling protocol will improve kriging and therefore the BME results.

4.3. Future applications and outlook

Ks is an essential parameter for dimensioning a TWW infiltration area; it allows evaluating the maximum TWW discharge load for a specific soil surface. Its main drawback however involves the difficulty in obtaining a sufficient number of Ks measurements (due to both time and financial costs) in field applications. The geophysics and BME approach proposed in this paper was initially suggested to solve such an issue. The method yields an accurate distribution of Ks by fusing 24 experimental measurements of Ks with the ERT method. Yet for infiltration area design, conducting 24 infiltration tests remains too expensive. Consequently, it can only be applied to those cases representing a serious risk for the environment. In order to overcome this method use limitation, we are proposing to focus future research efforts on combining ERT and infiltration tests with less time-consuming methods, e.g. dynamic penetrometer. The BME method could also be generalized to other soil parameters (e.g. WC) and applications, especially in the field of water resources management.

5. Conclusion

This article has proposed a new approach to obtain Ks spatial distribution based on the integration of ERT and infiltration test data in the BME method. This method allows for the fusion of point-specific data, with a null variance (Ks), and distributed data, with a specific variance (ER). We have adapted the BME method to the specificities of both geophysical and geotechnical datasets. The results of this study show that BME is a high-performance method producing maps with a lower variance than any of the other methods tested (kriging, petrophysical relationship). Indeed, BME offers a first-level Ks distribution as well as many new possibilities, namely: i) the development of a new multi-method approach to coupling geophysical and geotechnical methods, ii) application to other fields of geosciences, and iii) use of results in hydrodynamic modeling for TWW infiltration area design.

6. Bibliography

Attwa, M., Ali, H., 2018. Resistivity Characterization of Aquifer in Coastal Semiarid Areas: An Approach for Hydrogeological Evaluation. pp. 213–233. https://doi.org/10.1007/698_2017_210

500 Aubertheau, E., Stalder, T., Mondamert, L., Ploy, M.-C., Dagot, C., Labanowski, J., 2017. Impact of wastewater
501 treatment plant discharge on the contamination of river biofilms by pharmaceuticals and antibiotic
502 resistance. Sci. Total Environ. 579, 1387–1398. https://doi.org/10.1016/j.scitotenv.2016.11.136

503 Audebert, M., Oxarango, L., Duquennoi, C., Touze-Foltz, N., Forquet, N., Clément, R., 2016. Understanding
504 leachate flow in municipal solid waste landfills by combining time-lapse ERT and subsurface flow
505 modelling – Part II: Constraint methodology of hydrodynamic models. Waste Manag. 55, 176–190.
506 https://doi.org/10.1016/j.wasman.2016.04.005

507 Benz-Navarrete, M.A., Breul, P., Moustan, P., 2019. Servo-Assisted and Computer-Controlled Variable Energy
508 Dynamic Super Heavy Penetrometer. Geotech. Eng. XXI Century Lessons Learn. Futur. challenges 65–72.
509 https://doi.org/10.3233/STAL190024

510 Bisone, S., Clément, R., Forquet, N., 2017a. Une méthodologie couplant mesures géophysiques et ponctuelles
511 afin d'estimer la perméabilité d'un site destiné à l'infiltration d'eau usée traitée. Déchets, Sci. Tech.
512 https://doi.org/10.4267/dechets-sciences-techniques.3602

513 Bisone, S., Gautier, M., Masson, M., Forquet, N., 2017b. Influence of loading rate and modes on infiltration of
514 treated wastewater in soil-based constructed wetland. Environ. Technol. 38, 163–174.
515 https://doi.org/10.1080/09593330.2016.1185165

516 Bornand, M., Dejou, J., Michel, R., Roger, L., 1984. Composition minéralogique de la phase argileuse des Terres
517 noires de Limagne (Puy-de-Dôme). Le problème des liaisons argiles-matière organique. Agronomie.

518 Brunet, P., Clément, R., Bouvier, C., 2010. Monitoring soil water content and deficit using Electrical Resistivity
519 Tomography (ERT) – A case study in the Cevennes area, France. J. Hydrol. 380, 146–153.
520 https://doi.org/10.1016/j.jhydrol.2009.10.032

521 Chils, J.-P., Delfiner, P., 1999. Geostatistics: modeling spatial uncertainty , Wiley , New York . John Wiley & Sons,
522 Inc. https://doi.org/10.1002/9780470316993

523 Christakos, G., Serre, M.L., Bogaert, P., 2002. Temporal GIS: Advanced Functions for Field-Based Applications.

524 Christensen, R., 2018. Analysis of Variance, Design, and Regression Linear Modeling for Unbalanced Data,
525 Second Edition.

526 Clement, R., Fargier, Y., Dubois, V., Gance, J., Gros, E., Forquet, N., 2020. OhmPi: An open source data logger for
527 dedicated applications of electrical resistivity imaging at the small and laboratory scale. HardwareX 8,
528 e00122. https://doi.org/10.1016/j.ohx.2020.e00122

529 Clement, R., Moreau, S., 2016. How should an electrical resistivity tomography laboratory test cell be designed?
530 Numerical investigation of error on electrical resistivity measurement. J. Appl. Geophys. 127, 45–55.
531 https://doi.org/10.1016/j.jappgeo.2016.02.008

532 D. Carrière, S., Chalikakis, K., Danquigny, C., Torrès-Rondon, L., 2014. How Calculate DOI Index to Assess
533 Inverted ERT model? https://doi.org/10.3997/2214-4609.20142021

534 D'Or, D., Bogaert, P., Christakos, G., 2001. Application of the BME approach to soil texture mapping. Stoch.
535 Environ. Res. Risk Assess. https://doi.org/10.1007/s004770000057

536 Dezert, T., Palma Lopes, S., Fargier, Y., Côte, P., 2019. Combination of geophysical and geotechnical data using
537 belief functions: Assessment with numerical and laboratory data. J. Appl. Geophys. 170, 103824.
538 https://doi.org/10.1016/j.jappgeo.2019.103824

539 Douaik, A., Van Meirvenne, M., Tóth, T., 2005. Soil salinity mapping using spatio-temporal kriging and Bayesian
540 maximum entropy with interval soft data. Geoderma 128, 234–248.
541 https://doi.org/10.1016/j.geoderma.2005.04.006

542 Doussan, C., Ruy, S., 2009. Prediction of unsaturated soil hydraulic conductivity with electrical conductivity.
543 Water Resour. Res. 45. https://doi.org/10.1029/2008WR007309

544 Elrick, D.E., Reynolds, W.D., Tan, K.A., 1989. Hydraulic Conductivity Measurements in the Unsaturated Zone
545 Using Improved Well Analyses. Groundw. Monit. Remediat. 9, 184–193. https://doi.org/10.1111/j.1745-
546 6592.1989.tb01162.x

547 Farzamian, M., Monteiro Santos, F.A., Khalil, M.A., 2015. Application of EM38 and ERT methods in estimation of
548 saturated hydraulic conductivity in unsaturated soil. J. Appl. Geophys. 112, 175–189.
549 https://doi.org/10.1016/j.jappgeo.2014.11.016

550 Friedel, S., 2003. Resolution, stability and efficiency of resistivity tomography estimated from a generalized
551 inverse approach. Geophys. J. Int. 153, 305–316. https://doi.org/10.1046/j.1365-246X.2003.01890.x

552 Glover, P.W.J., 2016. Archie's law – a reappraisal. Solid Earth 7, 1157–1169. https://doi.org/10.5194/se-7-1157-
553 2016

554 Günther, T., 2004. Inversion Methods and Resolution Analysis for the 2D/3D Reconstruction of Resistivity
555 Structures from DC Measurements.

556 Günther, T., Rücker, C., 2011. Boundless electrical resistivity tomography, BERT.User Tutorial.

557 Hellman, K., Ronczka, M., Günther, T., Wennermark, M., Rücker, C., Dahlin, T., 2017. Structurally coupled
558 inversion of ERT and refraction seismic data combined with cluster-based model integration. J. Appl.
559 Geophys. 143, 169–181. https://doi.org/10.1016/j.jappgeo.2017.06.008

560 Lee, S.-J., Yeatts, K.B., Serre, M.L., 2009. A Bayesian Maximum Entropy approach to address the change of
561 support problem in the spatial analysis of childhood asthma prevalence across North Carolina. Spat.
562 Spatiotemporal. Epidemiol. 1, 49–60. https://doi.org/10.1016/j.sste.2009.07.005

563 Li, X., Shen, J., Tian, G., Zhong, Y., 2019. Data fusion for resolution improvement by combining seismic data with
564 logging data. J. Appl. Geophys. 166, 122–128. https://doi.org/10.1016/j.jappgeo.2019.04.020

565 Loke, M.H., 1999. Time-lapse resistivity imaging inversion, in 5th meeting of the environnemental and
566 Engeering Society European Section. Ed. Budapest, Hungary.

567 Loke, M.H., Chambers, J.E., Rucker, D.F., Kuras, O., Wilkinson, P.B., 2013. Recent developments in the direct-
568 current geoelectrical imaging method. Appl. Geophys. 135–156.

569 Mahapatra, S., Jha, M.K., Biswal, S., Senapati, D., 2020. Assessing Variability of Infiltration Characteristics and
570 Reliability of Infiltration Models in a Tropical Sub-humid Region of India. Sci. Rep. 10, 1515.
571 https://doi.org/10.1038/s41598-020-58333-8

572 Mallants, D., Volckaert, G., Labat, S., 2003. Parameters values used in the performance assessment of the
573 disposal of low level radioactive waste at the nuclear zone Mol-Dessel. Annexes to the data collection
574 forms for engineered barriers. SCK•CEN-R-3521, rev. 1.

575 Mastrocicco, M., Vignoli, G., Colombani, N., Zeid, N.A., 2010. Surface electrical resistivity tomography and
576 hydrogeological characterization to constrain groundwater flow modeling in an agricultural field site near

577 Ferrara (Italy). Environ. Earth Sci. 61, 311–322. https://doi.org/10.1007/s12665-009-0344-6

578 McKinley, J.W., Siegrist, R.L., 2011. Soil Clogging Genesis in Soil Treatment Units Used for Onsite Wastewater
579 Reclamation: A Review. Crit. Rev. Environ. Sci. Technol. 41, 2186–2209.
580 https://doi.org/10.1080/10643389.2010.497445

581 MEDDE, (MINISTÈRE DE L'ÉCOLOGIE DU DÉVELOPPEMENT DURABLE ET DE L'ÉNERGIE), 2015. Arrêté du 21
582 juillet 2015 relatif aux systèmes d'assainissement collectif et aux installations d'assainissement non
583 collectif, à l'exception des installations d'assainissement non collectif recevant une charge brute de
584 pollution organique inférieure ou ég. J. Off. LA RÉPUBLIQUE FRANÇAISE.

585 Morugán-Coronado, A., García-Orenes, F., Mataix-Solera, J., Arcenegui, V., Mataix-Beneyto, J., 2011. Short-term
586 effects of treated wastewater irrigation on Mediterranean calcareous soil. Soil Tillage Res. 112, 18–26.
587 https://doi.org/10.1016/j.still.2010.11.004

588 Olea, R.A., 2006. A six-step practical approach to semivariogram modeling. Stoch. Environ. Res. Risk Assess. 20,
589 307–318. https://doi.org/10.1007/s00477-005-0026-1

590 Radulescu, M., Valerian, C., Yang, J., 2007. Time-lapse electrical resistivity anomalies due to contaminant
591 transport around landfills. Ann. Geophys. VOL. 50. https://doi.org/10.4401/ag-3075

592 REYNOLDS, W.D., ELRICK, D.E., 1985. IN SITU MEASUREMENT OF FIELD-SATURATED HYDRAULIC
593 CONDUCTIVITY, SORPTIVITY, AND THE α-PARAMETER USING THE GUELPH PERMEAMETER. Soil Sci. 140,
594 292–302. https://doi.org/10.1097/00010694-198510000-00008

595 Richards, L.A., 1931. CAPILLARY CONDUCTION OF LIQUIDS THROUGH POROUS MEDIUMS. Physics (College.
596 Park. Md). 1, 318–333. https://doi.org/10.1063/1.1745010

597 Romero-Ruiz, A., Linde, N., Keller, T., Or, D., 2018. A Review of Geophysical Methods for Soil Structure
598 Characterization. Rev. Geophys. 56, 672–697. https://doi.org/10.1029/2018RG000611

599 Rücker, C., Günther, T., Wagner, F.M., 2017. pyGIMLi: An open-source library for modelling and inversion in
600 geophysics. Comput. Geosci. 109, 106–123. https://doi.org/10.1016/j.cageo.2017.07.011

601 Samouëlian, A., Cousin, I., Tabbagh, A., Bruand, A., Richard, G., 2005. Electrical resistivity survey in soil science:

602 a review. Soil Tillage Res. 83, 173–193. https://doi.org/10.1016/j.still.2004.10.004

603 Schaap, M.G., Feike, J.L., Van Genuchten, M.T., 2001. Rosetta: a computer program for estimating soil hydraulic
604 parameters with hierarchical pedotransfer functions. J. Hydrol. 251, 163–176.
605 https://doi.org/10.1016/S0022-1694(01)00466-8

606 Serre, M.L., Christakos, G., 1999. Modern geostatistics: computational BME analysis in the light of uncertain
607 physical knowledge - the Equus Beds study. Stoch. Environ. Res. Risk Assess. 13, 1–26.
608 https://doi.org/10.1007/s004770050029

609 Siegrist, R.L., 2014. Engineering design of a modern soil treatment unit. Innovations in soil-based onsite
610 wastewater treatment, in: Soil Society Society of America Conference Proceeding, Albuquerque (NM).

611 Telford, W.M., Geldart, L.P., Sheriff, R.E., 1990. Resistivity Methods, in: Applied Geophysics. Cambridge
612 University Press, Cambridge, pp. 522–577. https://doi.org/10.1017/CBO9781139167932.012

613 Vogelgesang, J.A., Holt, N., Schilling, K.E., Gannon, M., Tassier-Surine, S., 2020. Using high-resolution electrical
614 resistivity to estimate hydraulic conductivity and improve characterization of alluvial aquifers. J. Hydrol.
615 580, 123992. https://doi.org/10.1016/j.jhydrol.2019.123992

616 Warrick, A.W., Mullen, G.J., Nielsen, D.R., 1977. Predictions of the Soil Water Flux Based upon Field-measured
617 Soil-water Properties. Soil Sci. Soc. Am. J. 41, 14–19.
618 https://doi.org/10.2136/sssaj1977.03615995004100010009x

619 Weller, A., Slater, L., 2019. Permeability estimation from induced polarization: an evaluation of geophysical
620 length scales using an effective hydraulic radius concept. Near Surf. Geophys. 17, 581–594.
621 https://doi.org/10.1002/nsg.12071

622 Wunderlich, T., Petersen, H., Attia al Hagrey, S., Rabbel, W., 2013. Pedophysical Models for Resistivity and
623 Permittivity of Partially Water-Saturated Soils. Vadose Zo. J. 12, vzj2013.01.0023.
624 https://doi.org/10.2136/vzj2013.01.0023

625 Zhang, Hopkins, Guo, Lin, 2019. Dynamics of Infiltration Rate and Field-Saturated Soil Hydraulic Conductivity in
626 a Wastewater-Irrigated Cropland. Water 11, 1632. https://doi.org/10.3390/w11081632